THE SPIN AND ORIENTATION OF DARK MATTER HALOS WITHIN COSMIC FILAMENTS

Youcai Zhang[1,2], Xiaohu Yang[1], Andreas Faltenbacher[3], Volker Springel[3], Weipeng Lin[1], and Huiyuan Wang[4]
[1] Key Laboratory for Research in Galaxies and Cosmology, Shanghai Astronomical Observatory, the Partner Group of MPA, Nandan Road 80, Shanghai 200030, China; yczhang@shao.ac.cn
[2] Graduate School of the Chinese Academy of Sciences, 19A, Yuquan Road, Beijing, China
[3] Max-Planck-Institut für Astrophysik, Karl-Schwarzschild-Strasse 1, 85748 Garching, Germany
[4] Key Laboratory for Research in Galaxies and Cosmology, Center for Astrophysics, University of Science and Technology of China, 230026, China

ABSTRACT

Clusters, filaments, sheets, and voids are the building blocks of the cosmic web. Forming dark matter halos respond to these different large-scale environments, and this in turn affects the properties of galaxies hosted by the halos. It is therefore important to understand the systematic correlations of halo properties with the morphology of the cosmic web, as this informs both about galaxy formation physics and possible systematics of weak lensing studies. In this study, we present and compare two distinct algorithms for finding cosmic filaments and sheets, a task which is far less well established than the identification of dark matter halos or voids. One method is based on the smoothed dark matter density field and the other uses the halo distributions directly. We apply both techniques to one high-resolution N-body simulation and reconstruct the filamentary/sheet like network of the dark matter density field. We focus on investigating the properties of the dark matter halos inside these structures, in particular, on the directions of their spins and the orientation of their shapes with respect to the directions of the filaments and sheets. We find that both the spin and the major axes of filament halos with masses $\lesssim 10^{13}\ h^{-1}\ M_\odot$ are preferentially aligned with the direction of the filaments. The spins and major axes of halos in sheets tend to lie parallel to the sheets. There is an opposite mass dependence of the alignment strength for the spin (negative) and major (positive) axes, i.e. with increasing halo mass the major axis tends to be more strongly aligned with the direction of the filament, whereas the alignment between halo spin and filament becomes weaker with increasing halo mass. The alignment strength as a function of the distance to the most massive node halo indicates that there is a transit large-scale environment impact: from the two-dimensional collapse phase of the filament to the three-dimensional collapse phase of the cluster/node halo at small separation. Overall, the two algorithms for filament/sheet identification investigated here agree well with each other. The method based on halos alone can be easily adapted for use with observational data sets.

Key words: dark matter – galaxies: halos – large-scale structure of universe – methods: data analysis

Online-only material: color figures

1. INTRODUCTION

Inspection of the galaxy distribution in redshift surveys (e.g., in the Sloan Digital Sky Survey, SDSS; York et al. 2000) or of the distribution of dark matter particles in numerical simulations (e.g., Millennium Simulations; Springel et al. 2005) reveals a striking "cosmic web" (Bond et al. 1996), composed of clusters, filaments, sheets, and voids as primary building blocks. In the matter or galaxy distributions, one can clearly see large volumes of "empty" regions (voids) which are surrounded by thin denser sheet-like structures (sheets). At even higher density contrast a network of filaments dominates the matter or galaxy distributions. Finally, the massive clumps at the intersections of filaments typically correspond to rich galaxy groups and clusters. The human eye is readily capable of identifying these morphological features of the cosmic large-scale structure, but for quantitative analysis objective techniques for structure analysis are needed.

The most commonly employed statistical measure for the distribution of matter and galaxies is low-order clustering statistics (e.g., the two-point correlation function and its Fourier transform, the power spectrum; Peebles 1980). Apart from these standard statistical tools, one may also use other statistics, for example based on higher-order correlation functions, or measures for the abundance of halos as a function of mass or of voids of different sizes, to characterize the cosmic structure.

Since halos and voids are approximately spherically symmetric structures and relatively easy to model, several very successful methods to extract these structures from simulations and observations have been developed. In N-body simulations, halos are most commonly found as groups of particles by the friends-of-friends (FOF) algorithm with a linking length set equal to some fraction ($b \approx 0.2$) of the mean particle separation (e.g., Davis et al. 1985). Halos detected in this way show a mean enclosed density of about 180 times the average mass density of the universe. Observationally, galaxy groups can also be identified using the FOF method, but with two linking lengths in order to take redshift distortions into account (e.g., Eke et al. 2004). One may also use models for the density profile and velocity dispersion of dark matter halos to help extracting galaxy groups (e.g., Yang et al. 2005). There are numerous successful void finders, many of them have been compared in detail in a recent study by Colberg et al. (2009, and references therein).

Compared to clusters and voids, filaments and sheets are more complicated geometric structures. Both of them are genuine three-dimensional objects associated with a distinct orientation in space. Their density contrast is often quite close to the mean cosmic density, making their identification difficult and sometimes ambiguous. We also note that from a dynamical point of view there exists a sequence of transformations that can cast one of these structures into another, which blurs any clear distinction between these different morphological structures. Matter tends to flow out of the voids, then it accretes onto

the sheets, collapses to the filaments, and finally accumulates onto the large clumps at the intersection of the filaments. These processes are expected to impact the properties of the halos and the galaxies formed therein, leading to correlation between halo properties and large-scale environment. In a recent study, using high-resolution *N*-body simulations, Gao et al. (2005) found that the halo clustering strength not only depends on the masses of the halos but also on their formation times (see also Sheth & Tormen 2004; Wang et al. 2007; Dalal et al. 2008; Hahn et al. 2009). In addition to the age, other halo properties such as concentration and spin have also been found to correlate with the local environment (Avila-Reese et al. 2005; Wechsler et al. 2006; Bett et al. 2007; Gao & White 2007; Macciò et al. 2007).

Based on semi-analytical galaxy evolution models, Croton et al. (2007) showed that besides the properties of the host halo the large-scale environment has to be taken into account to fully characterize the galaxies at halo centers (see also Reed et al. 2007). Observations indicate a similar dependence of galaxy properties on environment. Using a large galaxy redshift catalog, Yang et al. (2006) showed that groups (of similar masses) with red central galaxies are more strongly clustered than those with blue central galaxies (see also Wang et al. 2008). Using the same data set, Wang et al. (2009b) detected numerous red dwarf galaxies which were isolated, i.e. which were not belonging to any neighboring larger association or group of galaxies. The origin of those red isolated dwarfs still remains unknown (see also Cooper et al. 2007). To shed some more light on the impact of the large-scale structure on halo/galaxy properties we here adopt the following strategy. We first identify and classify the large-scale environment, then we determine whether a given halo resides in a filament or sheet, and finally we try to find correlations between the halo spin and shape orientations and their large-scale environment.

Up to the present day, a number of different approaches have been suggested to find filaments (and/or sheets) in simulations as well as in observations. Among these methods two different classes of techniques can be distinguished: the first uses discrete distributions of objects (e.g., galaxies) and the second is based on continuous density fields. In the following, we briefly summarize the basic ideas of these two approaches (see also Aragón-Calvo et al. 2007a, and references therein).

A discrete point set allows the use of a minimum spanning tree technique to link the points (Barrow et al. 1985; Colberg 2007). However, cosmic structures identified by this method often show web-like features and it is difficult to define sizes and directions of the extracted filaments. Finding filaments joining neighboring clusters has also been carried out. Pimbblet (2005) searched the 2dF Galaxy Redshift Survey catalog for filamentary structures using the orientations of inter-cluster galaxies. A related approach based on the inter-cluster dark matter distribution derived from *N*-body simulations is discussed in Colberg et al. (2005). More mathematically, Stoica et al. (2005, 2007) used a so-called *Candy model* to locate the filaments in galaxy surveys. All these approaches have the advantage that they directly deal with the original point sources and do not require the creation of continuous density fields. However, in general these techniques incorporate a large number of free parameters and the specific assignment of these parameters is, to a certain degree, arbitrary.

The second type of techniques usually requires the creation of a continuous density field. These approaches include the full characterization of the topology of the matter distribution in terms of Minkowski functionals (Mecke et al. 1994; Schmalzing

et al. 1999), the genus of the density field (Gott et al. 1986; Hoyle & Vogeley 2002) and the shape-finder statistics in three (Sahni et al. 1998) and two dimensions (Pandey & Bharadwaj 2008). A more rigorous classification of filaments and other structural elements is obtained with the skeleton analysis of density fields by Novikov et al. (2006) and Sousbie et al. (2008), where the maxima and saddle points in the density field are specified using the Hessian matrix (i.e., the second partial derivative) of the density field. Recently, Hahn et al. (2007a, 2007b) have quantified the cosmic web using the Hessian matrix of the potential field where, according to the number of positive eigenvalues, a region was classified as belonging either to a cluster, filament, sheet, or void. The only free parameter in this analysis is the smoothing length of the density field. In a similar spirit, Aragón-Calvo et al. (2007a, 2007b) computed the Hessian matrix based on the density field constructed with a Delaunay triangulation field estimator (Schaap & van de Weygaert 2000).

The methods in this second category are mathematically more rigorous than the techniques based on discrete point sets. Only a few (or even no) free parameters are needed, and all halos (galaxies) can be classified since essentially every volume element and hence the objects within it can be classified. However, a disadvantage lies in the necessity for constructing a density (potential) field, and in the difficulties in assigning points, halos, or galaxies, to the appropriate volume element.

In this study, we compare two types of filament finding algorithms, one using the overall matter distribution and the other just the halos obtained from a high-resolution cosmological *N*-body simulation. Method I employs the Hessian matrix of the mass density field, where halos are differentiated into four types using a combination of criteria from Hahn et al. (2007b) and Aragón-Calvo et al. (2007a). Method II uses the halo distribution directly. Our development of this approach has been inspired by the Candy model approach suggested by Stoica et al. (2005) and the connecting cluster technique described in Colberg et al. (2005). Based on either method we extract filaments and sheets from our high-resolution *N*-body simulation. We then correlate the characteristics of the cosmic structures, such as sizes and orientations, with the spins and orientations of dark matter halos.

This paper is organized as follows. In Section 2, we give a brief description of our *N*-body simulation and the halo catalog we used. We present a detailed description of the filament-finding methods based on either the dark matter density field or the distribution of dark matter halos in Section 3. In Section 4, we analyze various alignment signal measurements for halos with respect to the filaments (and sheets). Finally, we summarize our results in Section 5.

2. *N*-BODY SIMULATIONS AND THE HALO CATALOG

2.1. Simulation Parameters and Halo Definition

In this study, we make use of a *N*-body simulation carried out at the Shanghai Supercomputer Center using the massively parallel GADGET2 code (Springel et al. 2001, 2005). The simulation evolved 1024^3 dark matter particles in a periodic box of 100 h^{-1} Mpc on a side from redshift $z = 120$ to the present epoch. The particle mass and softening length are 6.927×10^7 h^{-1} $M_\odot$ and 2.25 h^{-1} kpc, respectively. The cosmological parameters used in the simulation are $\Omega_m = \Omega_{dm} + \Omega_b = 0.25$, $\Omega_b = 0.045$, $h = 0.73$, $\Omega_\Lambda = 0.75$, $n = 1$,
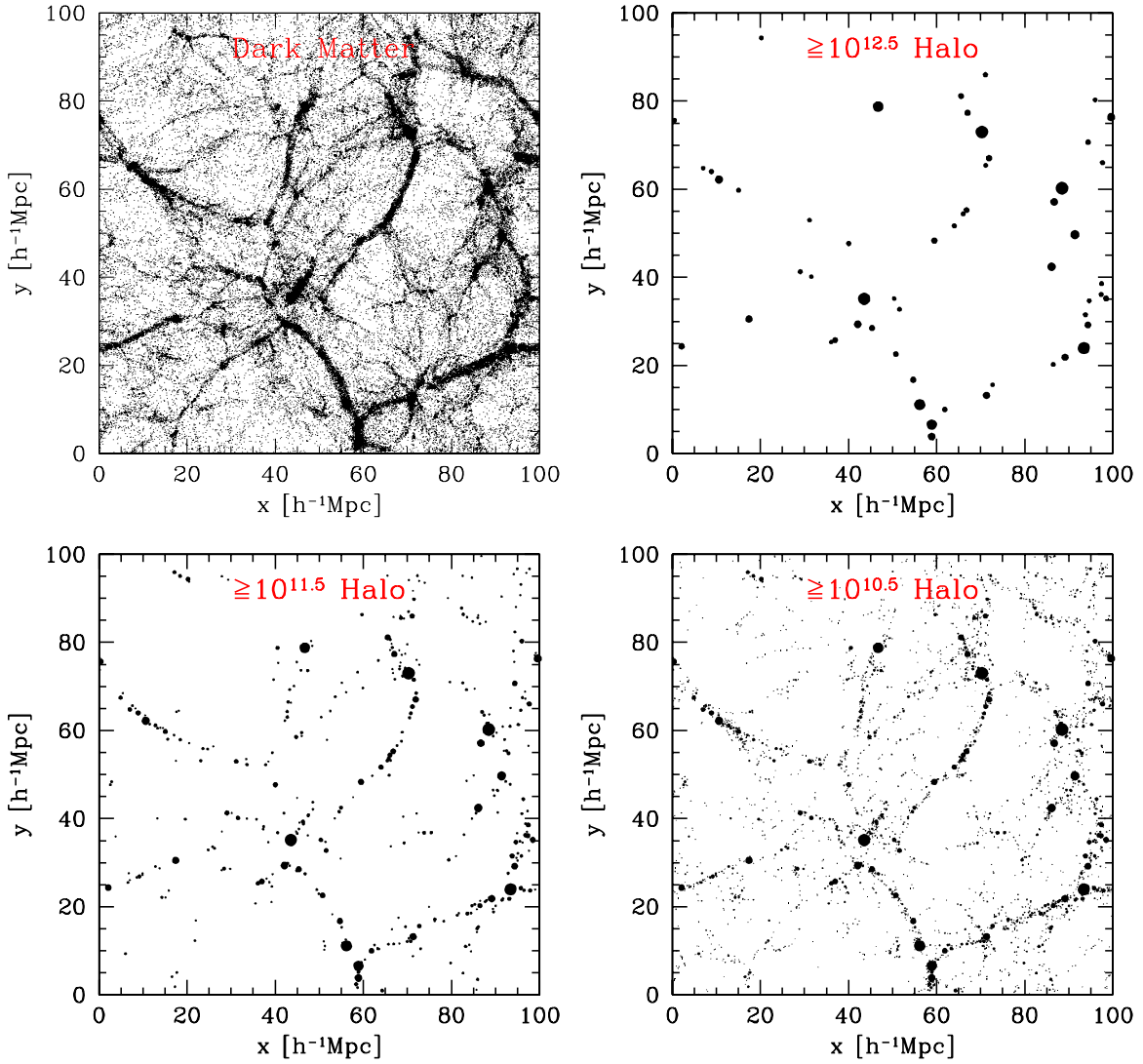
Figure 1. Dark matter (upper-left panel) and halo distributions in a slice of thickness 4 h^{-1} Mpc through the full box (100 h^{-1} Mpc on a side). For the halo distributions, the halo mass range (lower limit) is indicated in each panel, and the sizes of the dots are proportional to the virial radii of the halos.

and $\sigma_8 = 0.9$. In the upper-left panel of Figure 1, we show the distribution of dark matter particles in a slice of thickness 4 h^{-1} Mpc at redshift $z = 0$. For clarity, only 0.15% of the dark matter particles are plotted. This representation clearly shows the well-known features of the nonlinear cosmic density field, in particular, the prominent filamentary structures that coined the term "cosmic web" are nicely seen.

Dark matter haloes were identified from the simulation at redshift $z = 0$ using the standard FOF algorithm (Davis et al. 1985) with a linking length of 0.2 times the mean interparticle separation. Haloes obtained with this linking length have a mean over-density of ~ 180 (Porciani et al. 2002). As an illustration, we show in the upper-right, lower-left, and lower-right panels of Figure 1 the halo distributions for a sequence of decreasing lower mass limits: $\geqslant 10^{12.5}$, $\geqslant 10^{11.5}$, and $\geqslant 10^{10.5}$ h^{-1} $M_\odot$, as indicated in the panels. The sizes of the dots are scaled to be proportional to the virial radius of the dark matter halos. These plots indicate that the distribution of halos with masses $\geqslant 10^{12.5}$ h^{-1} $M_\odot$ can only resolve the high-density regions at the nodes of the cosmic web, while halos with masses $\geqslant 10^{11.5}$ h^{-1} $M_\odot$ trace the filamentary structures quite well. Including smaller halos down to $\geqslant 10^{10.5}$ h^{-1} $M_\odot$ can reveal subtle features even in void-like

regions. As discussed in Yang et al. (2009; Figure 1), the SDSS observations can completely resolve the dark matter halos with a mass limit of $\geqslant 10^{12.5}$ h^{-1} $M_\odot$ at redshift $z \sim 0.12$, and of $\geqslant 10^{11.5}$ h^{-1} $M_\odot$ at redshift $z \sim 0.05$. Thus, the halo-based probe for filamentary structures investigated in this paper can be reliably applied to the SDSS observations at low redshifts.

The main purpose of this paper is to probe the orientations and spins of dark matter halos with respect to the filaments and sheets within the cosmic web. However, a reliable measurement of these halo properties, in particular of the spin, requires high mass resolution. Therefore, we only retain halos with at least 500 particles for further analysis, resulting in a catalog with 73, 068 halos.

2.2. Measuring the Spin and Orientation of the Halos

The angular momentum $\boldsymbol{J}$ of a FOF halo containing N particles is

$$\boldsymbol{J} = m \sum_{i=1}^{N} \boldsymbol{r}_i \times \boldsymbol{v}_i, \tag{1}$$

where m is the particle's mass, $\boldsymbol{r}_i$ is the position vector of the ith particle relative to the center of mass, and $\boldsymbol{v}_i$ is its velocity relative to the bulk velocity of the halo.

In order to determine the shape of a FOF halo, we use the moment of inertia tensor[5] $\boldsymbol{I}$ with

$$I_{\alpha\beta} = m \sum_{i=1}^{N} x_{i,\alpha} x_{i,\beta}, \tag{2}$$

where $x_{i,\alpha}$ denotes the component α of the position vector of particle i with respect to the center of mass. The axis ratios a, b, and c ($a \geqslant b \geqslant c$) are proportional to the square roots of the corresponding eigenvalues, λ_1, λ_2, and λ_3, and the orientation of the halo is determined by the corresponding eigenvectors.

3. FINDING FILAMENTS IN THE N-BODY SIMULATION

In this section, we investigate two distinct methods to find the filaments in the simulation: one using the mass density field and the other using the distribution of dark matter halos.

3.1. Density Field Hessian Matrix Method

The first method we examine, hereafter referred to as Method I, is based on the local Hessian matrix H of the smoothed mass density field, defined as

$$H_{\alpha\beta} = \frac{\partial^2 \rho_s(\boldsymbol{x})}{\partial x_\alpha \partial x_\beta}, \tag{3}$$

where $\rho_s(\boldsymbol{x})$ is the smoothed density field. α and β denote the Hessian matrix indices with values of 1, 2, or 3. Thus, at the location $\boldsymbol{x}$ of each halo we can quantify the local "shape" of the density field by calculating the eigenvalues of the Hessian matrix (e.g., Aragón-Calvo et al. 2007a). The number of positive eigenvalues of $H_{\alpha\beta}$ can be used to classify the possible environments in which a halo can reside into four regions, according to:

1. *cluster*: a region with no positive eigenvalue;
2. *filament*: a region with one positive and two negative eigenvalues;
3. *sheet*: a region with two positive and one negative eigenvalues;
4. *void*: a region with three positive eigenvalues.

The direction of a filament can be identified with the eigenvector corresponding to the single positive eigenvalue of the Hessian matrix in a filament region. We note that this method has only one free parameter, namely the smoothing scale R_s of the Gaussian filter employed in constructing the density field. Different from the multi-scale morphology filter (MMF) method discussed in Aragón-Calvo et al. (2007a), we follow Hahn et al. (2007b) and adopt a fixed smoothing length of $R_s = 2.1 \ h^{-1}$ Mpc.

Hahn et al. (2007b) pointed out that the relative volume fractions of the four categories depend on the choice of R_s. For $R_s = 2.1 \ h^{-1}$ Mpc (corresponding to halo masses of

$\sim 10^{13} \ h^{-1} \ M_\odot$) they find a good agreement between their orbit-stability criterion and a visual classification of the large-scale structure.[6]

In order to compute the Hessian matrix $H_{\alpha\beta}$, we first construct a continuous density field from the discrete distribution of particles in the N-body simulation, using the cloud-in-cell (CIC) technique with a 1024^3 grid. Then the smoothed density field ρ_s is produced by smoothing the CIC generated density field ρ_{cic} with a spherically symmetric Gaussian filter G_{R_s},

$$\rho_s(\boldsymbol{x}) = \int d\boldsymbol{y} \, \rho_{\mathrm{cic}}(\boldsymbol{y}) G_{R_s}(\boldsymbol{y}, \boldsymbol{x}), \tag{4}$$

where $\boldsymbol{x}$ corresponds to the location of a given halo and the Gaussian filter with smoothing scale, R_s, is given by

$$G_{R_s} = \frac{1}{\left(2\pi R_s^2\right)^{3/2}} \exp\left(-\frac{|\boldsymbol{y} - \boldsymbol{x}|^2}{2R_s^2}\right). \tag{5}$$

From Equations (3)–(5), we find

$$H_{\alpha\beta} = \frac{1}{R_s^4} \int d\boldsymbol{y} \left[(x_\alpha - y_\alpha)(x_\beta - y_\beta) - \delta_{\alpha\beta} R_s^2\right]$$
$$\times \rho_{\mathrm{cic}}(\boldsymbol{y}) G_{R_s}(\boldsymbol{y}, \boldsymbol{x}), \tag{6}$$

where $\delta_{\alpha\beta}$ is the Kronecker delta (Aragón-Calvo et al. 2007a). Finally, the eigenspace structure of the symmetric Hessian matrix can be computed at the center of mass of each halo.

According to the number of positive eigenvalues at the locations of the dark matter halos we classify them into four categories, as outlined above. The numbers of halos in cluster, sheet, filament, and void regions are, respectively, 13,803, 13,230, 45,755, and 280, corresponding to 18.89%, 18.11%, 62.62%, and 0.38% of the total number of halos. In the left panel of Figure 2, we show the distribution of halos in a slice of thickness 4 h^{-1} Mpc, indicating the classification according to their environments with different colors. In addition, the directions of the filaments are marked with arrows for those halos associated with them. The right panel of Figure 2 shows the environmental classification of 256^2 grid point put down regularly in the mid-plane of the slice. According to visual inspection, the general appearance of the filamentary structures identified with this method is remarkably good.

3.2. Segment Extraction Method

As shown in the previous section, filamentary structures can be well identified using the Hessian matrix of the density field. However, this approach relies on an accurate knowledge of the matter density field, which is in many cases highly non-trivial to obtain. In particular, for observational data one may wish to use the distribution of galaxies, groups, or halos directly to identify the filaments of the cosmic web. For this purpose, we now present a halo-based method for filament finding which is based on a slightly modified version of the "Candy model" proposed

---

[5] Actually, Equation (2) represents the second moment of the mass tensor. The correct definition of the moment-of-inertia tensor deviates from this expression (see, e.g., Equation (1) in Hahn et al. 2007b). However, in the context of cosmological alignment studies it has become a convention to call the second moment of mass tensor and inertia tensor.

[6] Note, however, that Hahn et al. compute the Hessian matrix based on the gravitational potential field, ϕ, which is derived from the matter density distribution via Poisson's equation,

$$\nabla^2 \phi = 4\pi G \rho_s(\boldsymbol{x}),$$

where the Poisson's equation is solved using a fast Fourier transform on 1024^3 grid cells. As a consequence of that, their eigenvalues have opposite signs compared to those based on the corresponding density field that we use here.
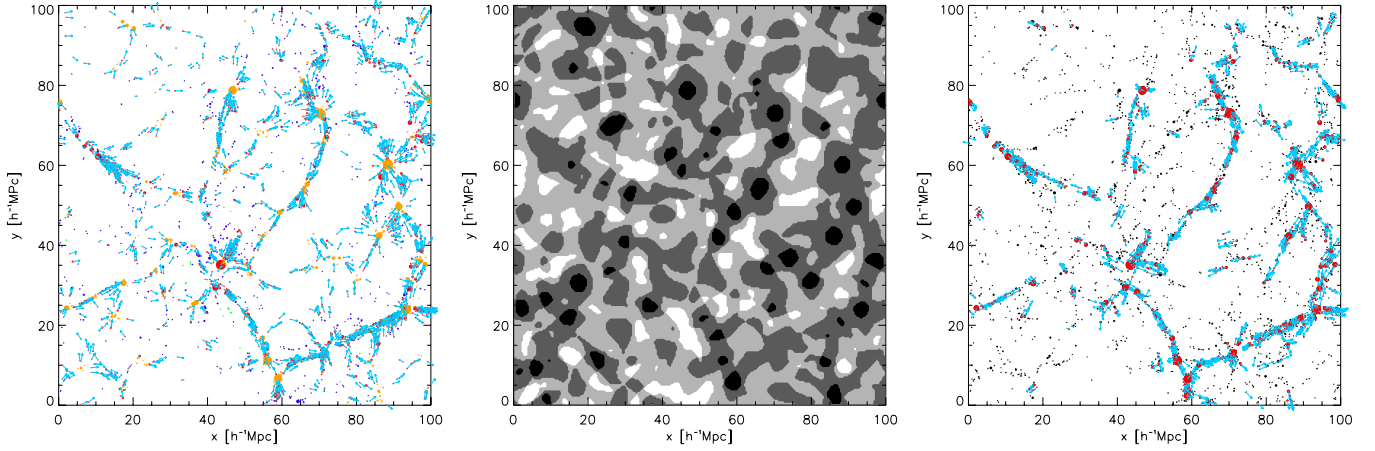
Figure 2. Halo distributions and environmental classifications. The left panel is similar to the lower-right panel of Figure 1, but for halos with at least 500 particles (i.e., $\geqslant 10^{10.54}\ h^{-1}\ M_\odot$). The halos in four different environments are classified by different colors: clusters (orange), sheets (blue), filaments (red), and voids (green). The cyan arrow indicates the direction of the filament at the center of each halo. The direction of the filament is given by the eigenvector corresponding to the single positive eigenvalue of the density Hessian matrix. The middle panel shows the environmental classifications of 256^2 grid points in the middle plane of the slice. Black corresponds to clusters, dark gray to filaments, clear gray to sheets, and white to voids. The right panel is similar to the left panel, but shown for filamentary structures identified using the segment extraction method (Method II). The halos in the filaments (both node and member halos) are plotted using red color. In addition, each member halo is also marked with an arrow indicating the direction of the filament it resides in.

(A color version of this figure is available in the online journal.)

by Stoica et al. (2005). The Candy model reconstructs filaments by connecting individual segments that are found in a basic point distribution (galaxies, halos, etc.). In this study, we only aim to compare halo shape orientations with the orientations of the segments they are residing in, thus we do not discuss in detail the problem of composing individual segments into long connected filaments. Hereafter, the segment extraction method derived from the Candy model will be referred to as Method II. In brief, there are two fundamental differences between Methods I and II. One is the use of a biased tracer of the density field in Method II. The other is that halos in Method II are automatically grouped into given filaments. That is, we know what halo belongs to what filament.

The requirements which a group of pointshave to fulfill to be considered a candidate segment have to be adjusted to the problem in question. Here, we focus on dark matter halos as building blocks for the filamentary structure of the cosmic web. Therefore, a candidate segment is assumed to be a cylinder, with a length in the range of $[L_{min}, L_{max}]$ and a radius in the range $[R_{min}, R_{max}]$. The mean mass density within the segment should be at least N_ρ times that of the average mass density of all halos, $\bar\rho_h = M_{h,tot}/V$, where $M_{h,tot}$ is the total mass of the halos with more than 500 particles and V is the volume of the simulation. Finally, a segment should have at least N_{min} member halos. We set these free parameters as follows:

$$
\begin{aligned}
L_{min} &= 3\ h^{-1}\ \text{Mpc}, \\
L_{max} &= 10\ h^{-1}\ \text{Mpc}, \\
R_{min} &= 1\ h^{-1}\ \text{Mpc}, \\
R_{max} &= 3\ h^{-1}\ \text{Mpc}, \\
N_\rho &= 5, \\
N_{min} &= 5.
\end{aligned}
\tag{7}
$$

Note that the values chosen for these parameters are somewhat arbitrary, but the results are robust to substantial changes in these parameters. In particular, we tested a number of different reasonable sets of parameter values, all of them led to general agreement between the results. Specifically, we found that

changing any of the above listed parameters (except for N_ρ) by 50% will only result in a less than 5% change in the number of halos identified as belonging to filaments. If N_ρ is varied to $N_\rho = 2.5$ or $N_\rho = 10.0$, about 59% or 31% of the halos, respectively, are classified as belonging to filaments. Even for these two cases, the final results do not change qualitatively, however.

In the following, we describe the successive steps of the segment extraction method.

Step 1. The dark matter halos are ranked according to their masses.

Step 2. Starting from the most massive halo to even smaller ones, we search around each halo i (node) all other halos j with distance in the range $[L_{min}, L_{max}]$. These halo pairs form candidates for our filament segments.

Step 3. We calculate for each candidate segment the filament strength (average mass density), $S_{i,j}$, which is defined as

$$
S_{i,j} = \sum_{k=1}^{N} M_k / \left(\pi R_s^2 L_{i,j} \right).
\tag{8}
$$

Here, $L_{i,j}$ is the length of the candidate segment (distance between the two halos i and j), N is the total number of halos within the cylinder around this segment with radius R_s, and M_k is the mass of halo k. The candidate segment radius, in the range $R_s \in [\max(R_{min}, r_{vir,i}), R_{max}]$, is determined such that $S_{i,j}$ reaches its maximum.

Step 4. For all the candidate segments, we rank their strength $S_{i,j}$. The one with the largest strength, with at least N_{min} member halos and $S_{i,j} \geqslant N_\rho \bar\rho_h$, is defined as the first candidate segment associated with node halo i.

Step 5. We rank all the member halos within that segment according to their masses, except the node halo i. The most massive one l with at least $N_{min} - 2$ halos residing between halos i and l is defined as the second, terminal node of the segment. We remove those member halos that are between the two node halos (belonging to segment i, l) from the halo list. Thus, member halos can only belong to one segment, while node halos can belong to more than one segment. The direction of the
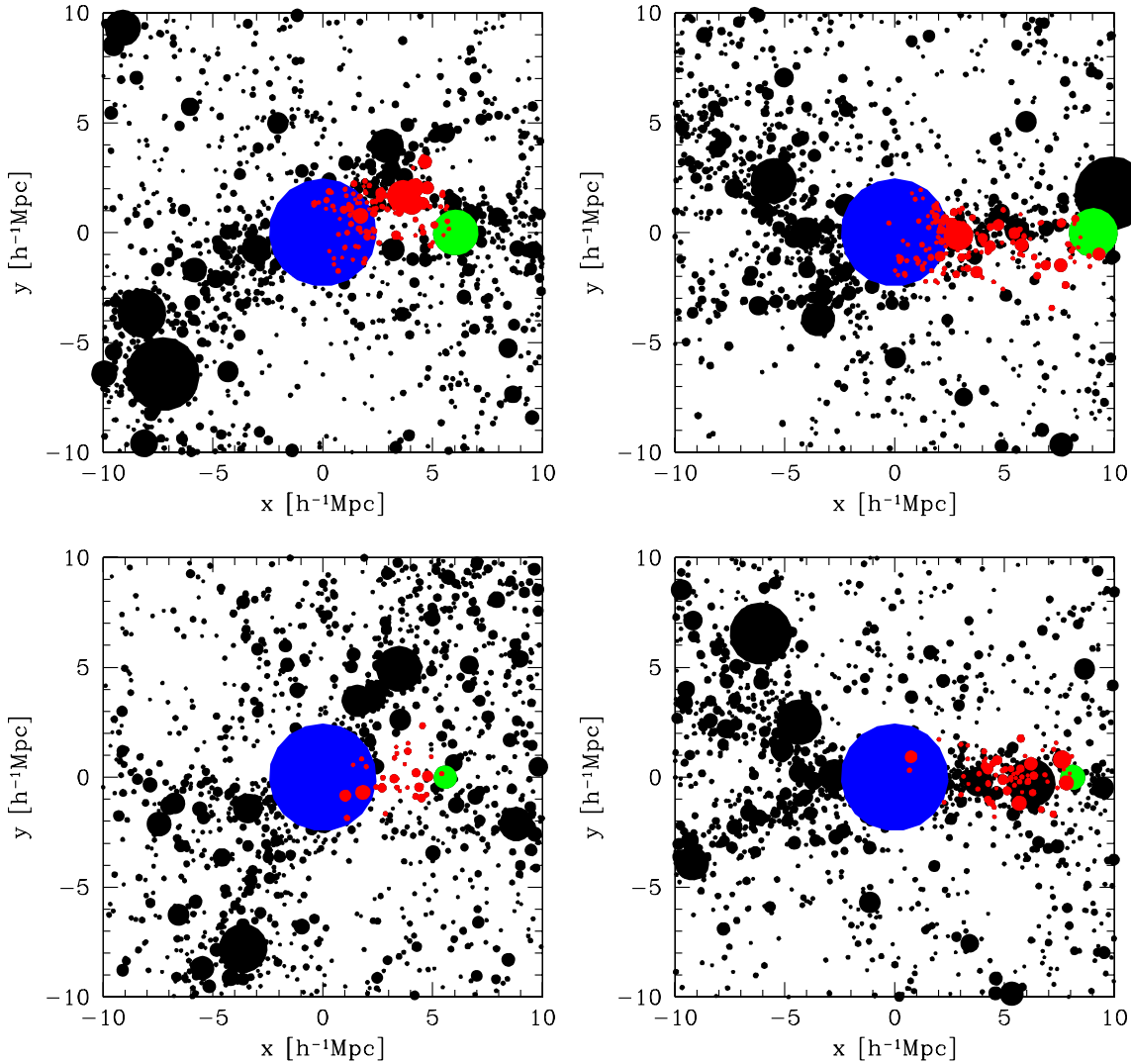
Figure 3. Distribution of dark matter halos around the most massive halo in our simulation, where only halos with at least 500 particles and within a $(20\ h^{-1}\ \mathrm{Mpc})^3$ box centered at the most massive halo are plotted. In each panel, the colored halos are within one filamentary segment: blue, starting node halo; green, ending node halo; red, member halos. Four segments in a total of six associated with the most massive halo are shown in four panels. For better visual quality, the distributions of halos are rotated so that the segment is always displayed along the x-axis.

(A color version of this figure is available in the online journal.)

segment (filament) is defined to be the connecting line between the two node halos.

Step 6. Once the segment (i, l) is determined, we return to step 1 and search for other segments associated with node halo i until no further segments can be found for this node halo. As an illustration, we show in Figure 3 the halo distribution in a $(20\ h^{-1}\ \mathrm{Mpc})^3$ cube centered on the most massive halo $i = 1$, together with the node and member halos in segment (i, l) which are marked with colored dots. The first four segments associated with node halo i (6 in total) are illustrated using colored dots in the four panels of Figure 3.

Step 7. We turn to the next node halo to search for its associated segments. We iteratively search the halo catalog until no further segments can be found.

Applying the segment extraction method to our halo catalog we find that 45% of all halos are classified as members of segments and 2% as node halos. These two populations are substantially smaller than those obtained with Method I, where we found 63% and 19% to be classified as filament and cluster halos, respectively. Note, however, in a recent paper, Forero-

Romero et al. (2009) introduced an additional threshold λ_{th} for the classification of environment instead of just using the number of positive (negative) eigenvalues. Increasing this barrier from $\lambda_{\mathrm{th}} = 0$ to some finite value greatly reduces the volume (mass) occupied by the identified filaments, and in particular, reduces the number of ambiguous detections of feeble or spurious filaments. The discrepancy may hence just be a result of the higher detection threshold of Method II compared with Method I. As a more quantitative comparison, in Figure 4, we show the mass functions of filament halos derived with Method I (red dashed) and Method II (green dotted). The mass functions obtained from the two methods are very similar, especially at the high-mass end. While at the low mass end, because of the higher detection threshold of Method II, less halos are specified as belonging to the filaments. For reference, we also show the total mass function from our simulation (blue dash-dotted), which is in good agreement with the analytic model prediction by Sheth et al. (2001; SMT, black solid).

The right panel of Figure 2 shows the distribution of halos within the filaments obtained with Method II in a slice of
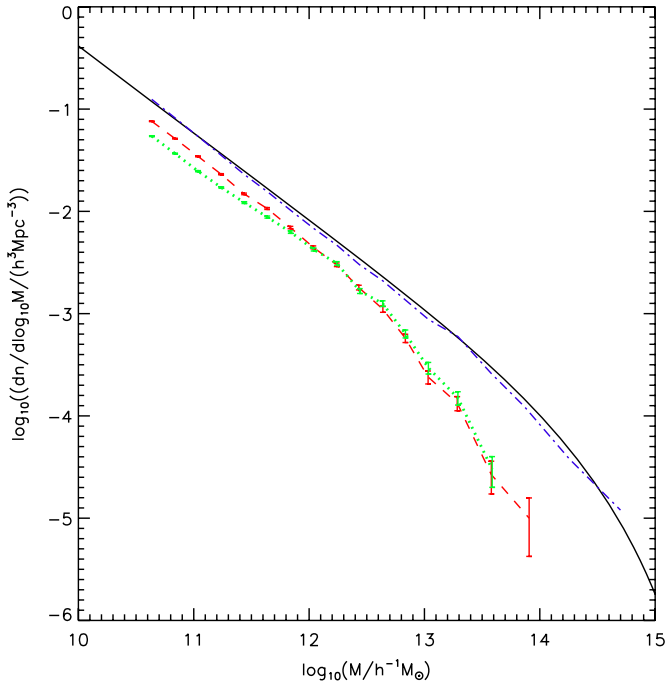
Figure 4. Mass function of the FOF halos residing in filaments in Method I (red dashed) and Method II (green dotted). Poisson error bars are added to assess the difference between the two methods. The filament mass function is scaled to the whole volume of our simulation. For comparison purposes, we also show the total mass function from our simulation (blue dash-dotted) and SMT analytic model prediction (black solid).

(A color version of this figure is available in the online journal.)

thickness $4\ h^{-1}$ Mpc. Compared to the filaments detected by the Hessian matrix approach in the left panel, only strong filaments are extracted by this method, while less prominent structures are not identified. Yet, the advantage of this method is that it does not require knowledge of the density field. This is a significant advantage especially in the context of observations, where density reconstruction is often difficult.

4. ORIENTATIONS OF DARK MATTER HALOS RELATIVE TO FILAMENTS AND SHEETS

To quantify the impact of filaments and sheets onto halos, we investigate two types of alignment signals: one based on a halo's spin and the other on its orientation. These two vectors correlate with the orientation of the filament or the normal vector of the sheet in which the halo resides. Finally, we also compare the results of the two filament-finding methods considered here. For simplicity, we will often use the terms "shape" and "spin," as well as "filament" and "sheet," as an indication of the direction in the obvious sense.

4.1. Statistical Methodology

In order to quantify the spin and shape orientations of halos relative to filaments, we compute the probability distribution function $P(\cos\theta)$ (alignment signal), where θ is the angle between the orientations of halo and filament or sheet,

$$P(\cos\theta) = N(\cos\theta)/\langle N_R(\cos\theta)\rangle. \qquad (9)$$

Here, $\cos(\theta)$ is restricted to the range $[0, 1]$, and $\cos(\theta) = 1$ implies that the halo orientations are parallel to the filaments while $\cos(\theta) = 0$ indicates perpendicular orientations. For the

null hypothesis of random orientations of halos relative to the environment one expects $P(\cos\theta) = 1$.

To assess the Poisson sampling errors in our alignment signals, we generate 500 random samples in which the orientations of filaments are kept fixed, but the halo spin or major axes orientations are randomized. For each of these samples we compute the $P_R(\cos\theta)$, which we use to compute the significance of any detected alignment signal.[7] In addition, we also calculate the mean cosine $\langle\cos(\theta)\rangle$ of the alignment angle. In the absence of any alignment, $\langle\cos(\theta)\rangle = 0.5$. The significance of any alignment can be assessed in terms of $\langle\cos(\theta)\rangle$ and $\sigma_{\cos(\theta)}$, which is the standard deviation of $\langle\cos(\theta)\rangle_R$ for the 500 random samples.

4.2. Spin–Filament Alignment

We first examine possible alignment signals between the spin of halos and the filaments they reside in. Method I, which is based on the Hessian matrix, allows us to distinguish cluster, sheet, filament, and void halos. For filament halos, the eigenvector of the positive eigenvalue of the Hessian matrix at the location of the halo indicates the direction of the filament. Method II determines the direction of the filament for each member halo in a segment as the connecting line between the two terminal node halos of that segment.
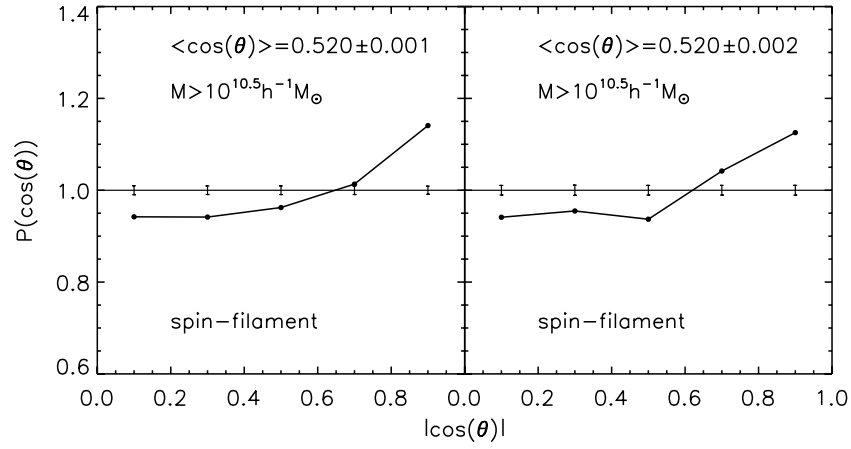
Figure 5 shows the probability distribution $P(\cos\theta)$ of the cosine of the angle between the halo spins and the filaments. The left and right panels display the results for Methods I and II, respectively. We find that the halo spins tend to lie parallel to the filaments. The results are robust against the filament detection method. It has been argued that the angular momentum of halos originates from the tidal field exerted by the surrounding dark matter distribution (Peebles 1969; Doroshkevich 1970; White 1984). The spin directions are expected to be preferentially aligned with the planes of the sheets and the directions of the filaments (e.g., Lee 2004), although hydrodynamical simulations have also suggested that the spin axis may align with the intermediate axis at turnaround (Navarro et al. 2004).

In order to characterize the strength of the alignment between angular momenta and filaments we calculate their average cosine, $\langle\cos(\theta)\rangle$. These average values together with their errors are displayed in the panels of Figure 5. Although the alignment signals for the two methods are slightly different, the overall strength of the alignment detected with Methods I and II agrees well.

Another interesting question is whether the alignment signal and strength depend on the mass of the filament halos. Figure 6 presents the probability distribution $P(\cos\theta)$ for filament halos in different mass ranges. Results are shown for Methods I and II in the upper and lower panels, respectively. The overall alignment signals obtained from the two methods are very similar. There is a weak mass dependence, in the sense that the alignment is somewhat weaker for massive halos. According to the values of $\langle\cos(\theta)\rangle$, filament halos with masses $M > 10^{12}\ h^{-1}\ M_\odot$ are consistent with being randomly oriented at a 2σ confidence level.

In a recent study, Hahn et al. (2007a) reported that the spin of halos with mass greater than the characteristic halo mass tends to lie perpendicular to the host filaments. This trend has been confirmed by Aragón-Calvo et al. (2007b).

---

[7] Since the significance of the alignment signals is quantified with respect to the null hypothesis, that is at which level it deviates from no alignments, throughout this paper, we plot the error bars on top of $P_R(\cos\theta) = 1$ lines.

Figure 5. Probability distribution of the cosine of the angle between the halo angular momentum vector and the direction of the filament in Methods I (left panel) and II (right panel). The error bars are computed from 500 random samples in which we randomize the orientations of the angular momenta of the halos. In case the angular momenta are randomly oriented, we would expect to find $P(\cos\theta) = 1$. Thus, the error bars are plotted on top of this $P(\cos\theta) = 1$ line. We also calculate the average value of $\cos(\theta)$, and its error, which are given in each panel.
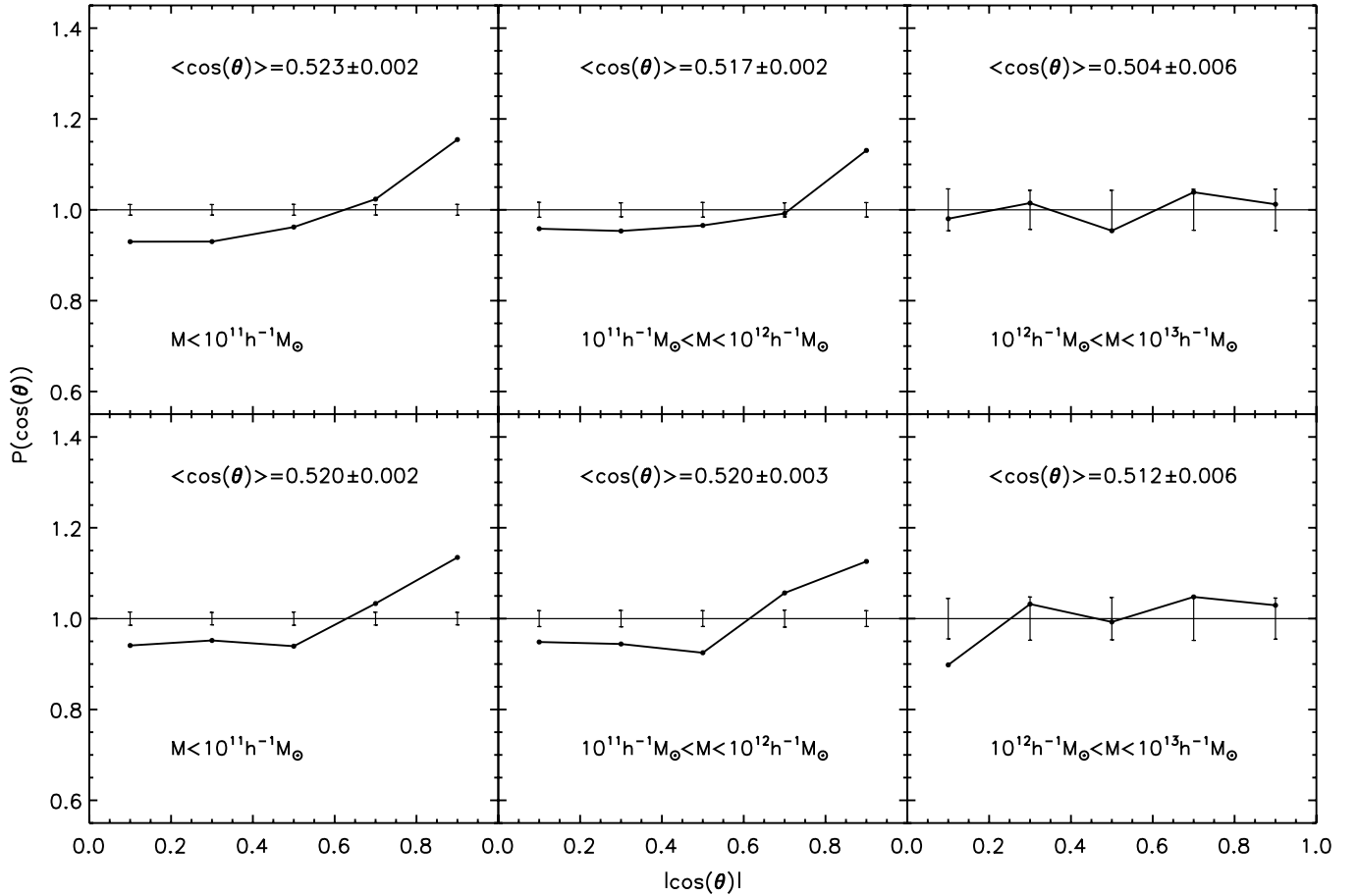
Figure 6. Same as Figure 5 but for different mass ranges of halos in the filaments in Methods I (upper panels) and II (lower panels). The average value of $\cos(\theta)$ and its error in each mass bin is indicated in each panel.

In a study comparing simulations and observations Paz et al. (2008) found an indication of this behavior based on SDSS data. The characteristic mass for gravitational collapse at redshift $z = 0$ is $9.57 \times 10^{12}\ h^{-1}\ M_\odot$, calculated for the cosmological parameters used in our simulation. Due to the small box size of our simulation, we find less than 100 filament halos with mass $\geqslant 10^{13}\ h^{-1}\ M_\odot$, independent of the filament finding method applied. Most of these massive halos are classified as clusters or node halos. Owing to the sparse number of filament halos, the statistics is too poor to obtain a robust measurement of the alignment signal, especially with respect to a possible transition from alignment to anti-alignment. However, for the well-constrained halo mass ranges $\leqslant 10^{13}\ h^{-1}\ M_\odot$, our alignment signals and strength are in very nice agreement with those found by Hahn et al. (2007a), and slightly larger than those predicted by Aragón-Calvo et al. (2007b).
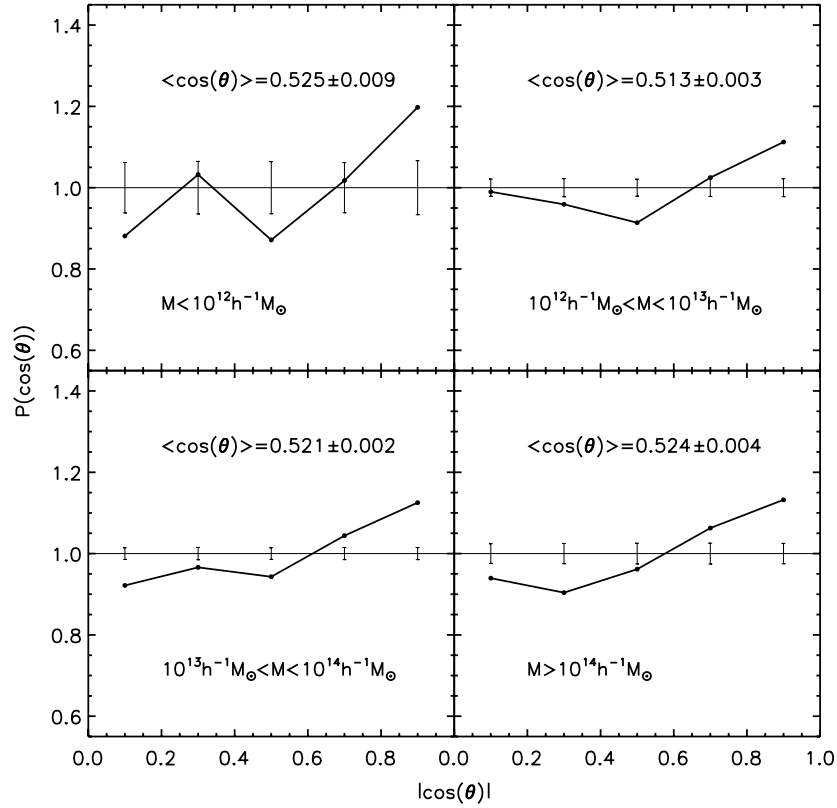
Figure 7. Same as Figure 5, but for halos in different segments in Method II, separated according to the mass of the most massive halo in each segment.

In Method II, the filaments are defined via segments extracted from the distribution of dark matter halos. Associated with each segment, there are two node halos, one of which is the most massive one among all the associated halos. Thus, we can probe the alignment signals separately for halos in filaments with different most massive node halos. In Figure 7, we show the results for four mass bins. There is a hint for a very weak positive mass dependence on the most massive halo in the segment, but this is statistically not significant. In addition to the mass dependence itself, we can further investigate the alignment signals at different separations to the most massive halo. The solid line in Figure 8 displays the alignment signals, the mean cosine of the angle between the spin and filament, for halos at different distances. We find that the strength of the alignment is slightly suppressed if the halos are either very close to or far away from the most massive node halos. To better understand this, we also measure the alignment signals for the mean cosine of the angle between spin and direction of the most massive node halo. The results are shown in Figure 8 as the dotted line. At large separation, since the direction of the most massive node halo and the filament direction is almost parallel, the two kinds of alignment signals are very similar. At very small separation, however, the spin and direction of the most massive halo show opposite alignment signal compare to that between the spin and filament. This feature clearly indicates a *transition* of the two-dimensional collapse phase of the filaments to the three-dimensional collapse phase of the cluster/node halos at small separation.

4.3. Shape–Filament Alignment

Next, we probe another important structural parameter, the orientation of the halo shape with respect to the direction of the filament. Similar to the last section, we measure the
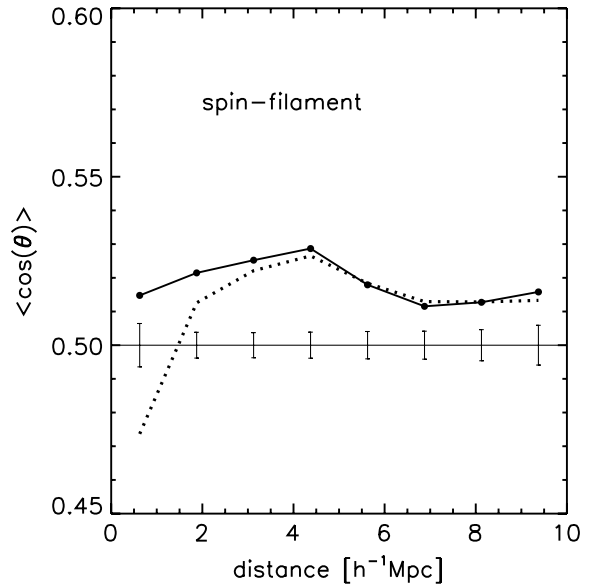
Figure 8. Mean cosine of the angle between spin and filament (solid line), between spin and direction of the most massive node halo (dotted line), as a function of the separations to the massive node halos in Method II.

alignment signals between the shapes and filaments for filament halos.

In Figure 9, we show the probability distribution of the cosine of the angle between the halo major axis and the direction of the filament. The left and right panels show the results for Methods I and II, respectively. We find significant alignment signals with both methods. In fact, the shapes of dark matter halos tend to be parallel to the filaments. Again, we use the average value of $\langle \cos(\theta) \rangle$ to quantify the strength of the alignment signal.
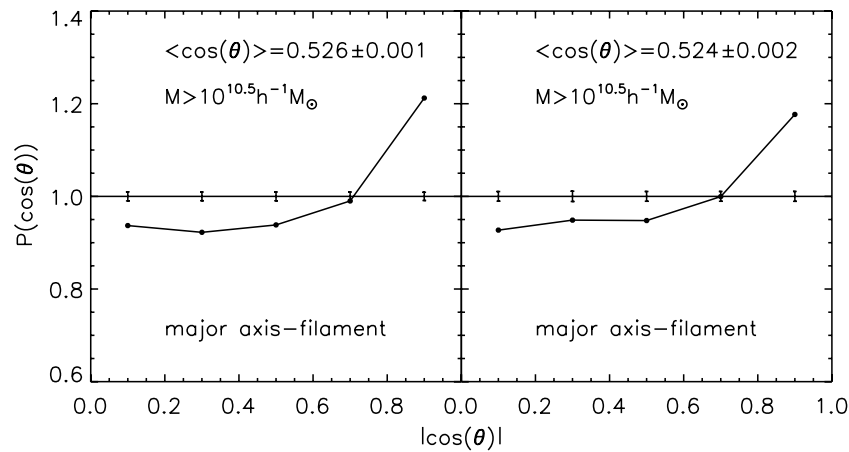
Figure 9. Probability distribution of the cosine of the angles between the halo major axis vectors and the directions of the filaments in Methods I (left panel) and II (right panel).

From Method I, we obtain an average cosine of 0.526 ± 0.001, whereas Method II results in a slightly smaller value of 0.524 ± 0.002. Similar alignment trends are reported in other recent studies (e.g., Altay et al. 2006; Aragón-Calvo et al. 2007b; Hahn et al. 2007a).

In analogy to our investigation of spin–filament alignment, we now examine the dependence of the alignment strength on mass and separation. Figure 10 shows the results for the filament halos in three mass bins. The upper and lower panels display results derived with Methods I and II, respectively. The strength of the alignment grows significantly with halo mass. Interestingly, the observed mass dependence shows an opposite trend compared to the spin–filament alignment. These trends agree well with results obtained by Hahn et al. (2007a) and Aragón-Calvo et al. (2007b).

In Figure 11, we show the alignment signals for halos in segments with most massive halos in four mass bins (note that this can only be done for Method II). An obvious mass dependence of the alignment signals is visible. Halos in segments with more massive node halos exhibit stronger alignment signals. The solid line in Figure 12 displays the alignment signals between shape and filament for halos at different separations to the most massive node halo. One can see a pronounced distance dependence. Halos at smaller separations to the most massive node halos, except at the smallest distance bin, tend to have stronger alignment strength. Similar to the spin of the halos, we also measure the alignment signals between shape and direction of the most massive node halo. The results are shown in Figure 12 as the dotted line. Obviously in this measure the distance dependence is much enhanced and *monotonic*. Again, this feature indicates the *transition* of the two-dimensional collapse phase of the filaments to the three-dimensional collapse phase of the cluster/node halos at small separation. This distance dependence, if not restricted to the filament members, is in general agreement with the alignment signals measured by Faltenbacher et al. (2008) for central and satellite halos as a function of radius and Pereira et al. (2008) for substructures with their host halos.

4.4. Spin–Sheet and Shape–Sheet Alignment

Method I differentiates between four cosmic environments: clusters, filaments, sheets, and voids. Filaments are distinguished by the condition that their Hessian matrix has only one single positive eigenvalue, and the corresponding eigenvector determines a unique direction. Sheets on the other hand are defined by having only one single negative eigenvalue. The associated eigenvector also determines a unique direction, which can be identified with the normal to the sheet.

The alignment signal for the angle between the halo spin and the normal of the sheet is shown in the left panel of Figure 13. We obtain an anti-alignment signal, which means that there is a trend for sheet halos to have their angular momentum vector parallel to the plane of the sheet. The alignment strength, quantified by the average of the cosine is $\langle \cos(\theta) \rangle = 0.473 \pm 0.002$. This alignment strength is in very good agreement with that obtained by Aragón-Calvo et al. (2007b).

The right panel of Figure 13 shows the probability distribution of the cosine of the angle between the halo major axis vector and the vector perpendicular to the sheet. The major axes of halos in sheets are strongly aligned with the sheet planes. The average of the cosine is 0.466 ± 0.002. A similar tendency has also been found in the shells of voids, as reported by Brunino et al. (2007).

4.5. Spin–Shape Alignment

Having specified the spin and shape (major axis) alignments with respect to the large-scale environments (filaments and sheets), we now proceed to examine the spin–shape alignment within the halos themselves. Figure 14 shows the alignment signals between the spin-major axes (left panel), spin-middle axes, (middle panel) and spin-minor axes (right panel), respectively. Measurements of these signals in different environments are displayed with different line styles: results are given for clusters (orange dotted), filaments (red dash-dotted), sheets (blue dashed), voids (green dash-dot-dot), and for all halos (black solid). In each case, the average of the cosine of the alignment angle is also indicated in each panel.

We find no significant environmental dependence of the alignment signal between the spin and shape of halos. The halo spin vector appears to be preferentially perpendicular to the halo major axis and has a strong tendency to be parallel to the halo minor axis. This behavior is in good agreement with previous findings obtained, e.g., by Faltenbacher et al. (2002), Bailin & Steinmetz (2005), Allgood et al. (2006), and Bett et al. (2007). We have also separately investigated the alignment signal for halos with mass $\leqslant 10^{11.0} \ h^{-1} \ M_\odot$ and $\geqslant 10^{12.5} \ h^{-1} \ M_\odot$, and basically found no dependence on mass besides a marginal enhancement of the alignment signal for the $\geqslant 10^{12.5}$ halos.
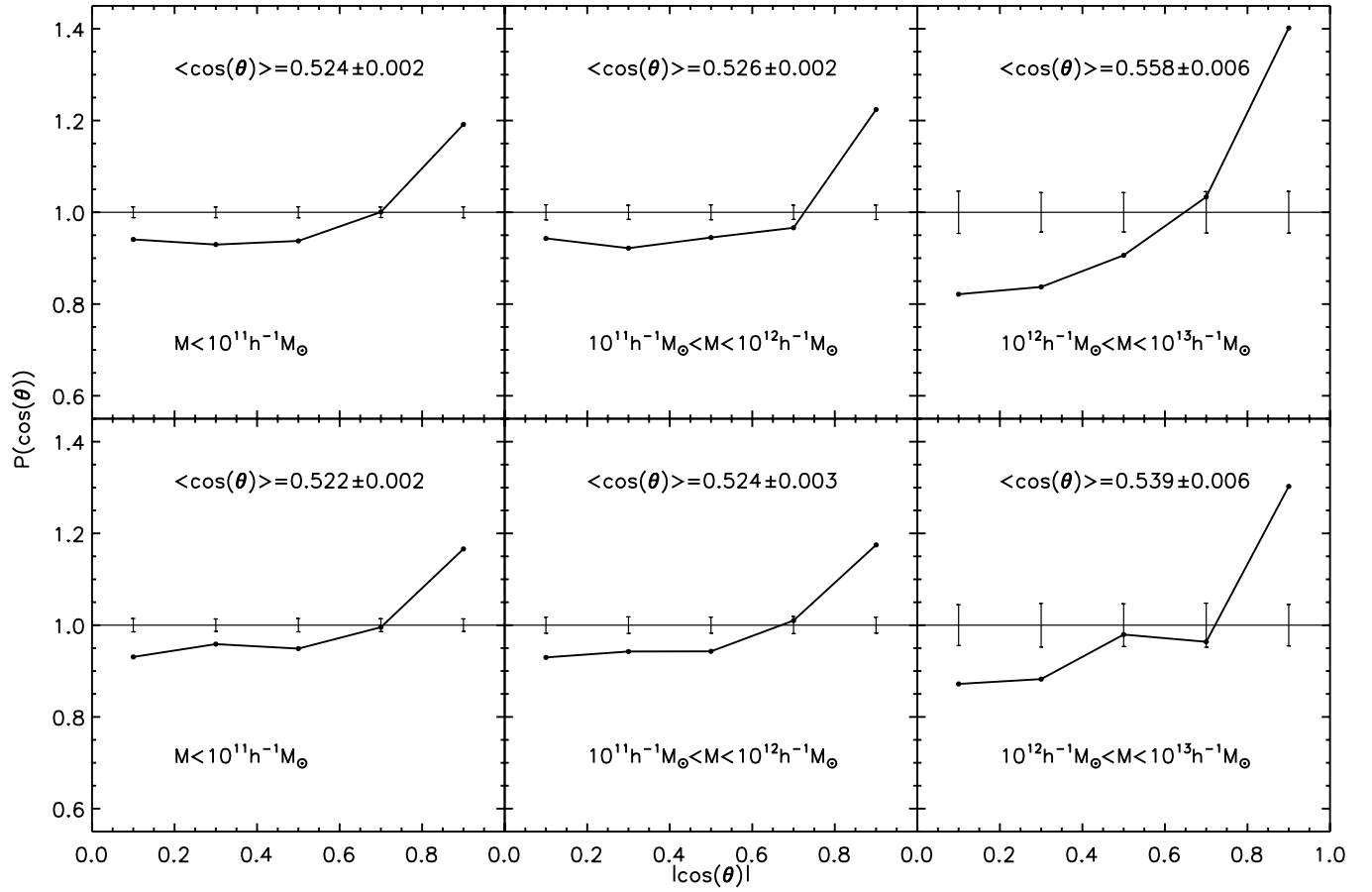
Figure 10. Same as Figure 9 but for different mass ranges of halos in the filaments in Methods I (upper panels) and II (lower panels), as indicated.
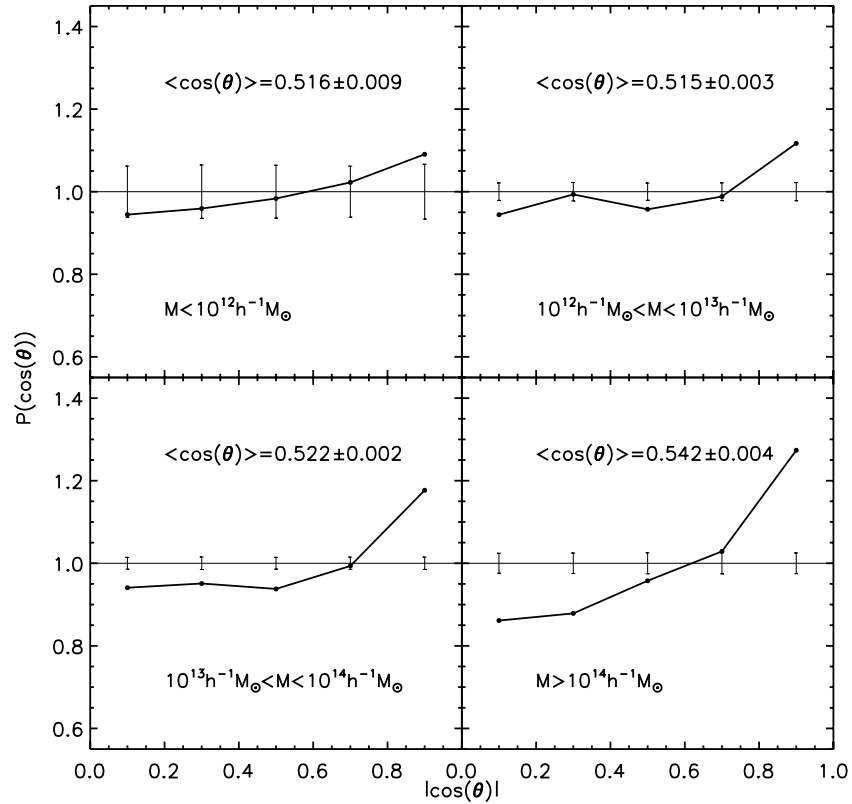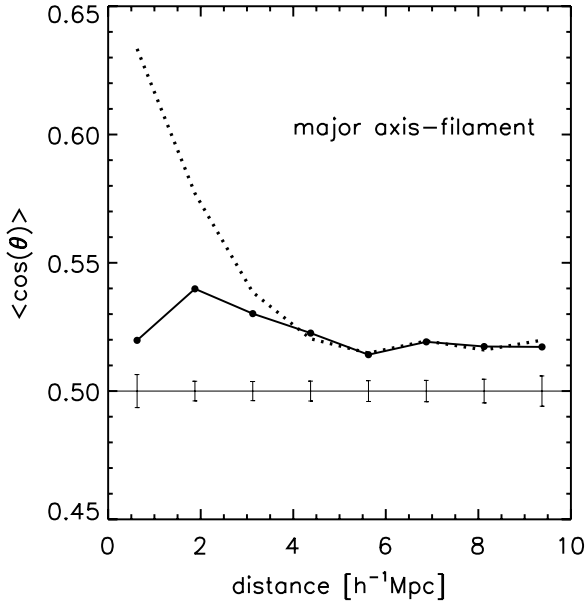

Figure 11. Same as Figure 9 but for halos in different segments in Method II, separated according to the mass of the most massive halo in each segment.

Figure 12. Mean cosine of the angle between shape and filament (solid line), between shape and direction of the most massive node halo (dotted line), as a function of the separations to the massive node halos in Method II.

According to our analysis above, both the spin and the major axes of halos are preferentially aligned with the directions of the filaments or the planes of the sheets. On the other hand, within halos the spin axes are strongly aligned with the *minor axes* of the halos. At first glance, these two results seem contradictory. In the case of a perfect alignment between halo spin and minor axes, an alignment between halo orientations and filaments would cause an anti-alignment between spin axes and filaments.

To have a better understanding of these two sets of "contradictory" results, we perform the following additional test. We first rank all the (member) halos within the filaments according to the cosine of their angles between the major axes and the filament directions, $\cos(\theta_1)$.[8] These halos are then split into four bins with equal numbers according to the values of $\cos(\theta_1)$. We then measure the cosines of the angles between the spin axis and the filament directions for the halos in each $\cos(\theta_1)$ bin. The results are shown in Figure 15, with upper panels for Method I

---
[8] To avoid the duplicated use of notation θ, here we use θ_1 to represent the angle between the major axis and the filament directions.

and lower panels for Method II. Each panel in Figure 15 from left to right corresponds to results for 1/4 of the halos in the filaments within a different $\cos(\theta_1)$ range, as indicated.

The most right-hand panels of this figure clearly demonstrate that a *strong* alignment between the major axes and the directions of the filaments produces an anti-alignment between the spin axes and the filaments. This result is in agreement with simple geometric considerations. Note however, theoretically a *strong* anti-alignment between the major axes and the directions of the filaments, as addressed in the left-hand panels of Figure 15, *does not* guarantee an alignment between the spin axes and the filaments. In the case of $\theta_1 = 90°$ and perfect alignment between minor axis and spin, the angle between the spin (minor) axis and the filament direction can assume any value within $0°$–$90°$. The very strong alignment signals apparent in the most left-hand panels must be induced purely by the influence of the filaments. Combining the signals from the four panels, one would obtain the alignment signals shown in Figure 5. On the other hand, note the range of the $\cos(\theta_1)$ in each panel, the average $\cos(\theta_1)$ for all halos in the four panels is larger than 0.5, again indicating an alignment between the major axis and filament directions (as shown in Figure 9). Thus, we conclude that the two sets of alignments are indeed not contradictory, and that the large-scale environment, i.e., the filaments and the sheets, can impact both the orientation and the spin of halos while allowing still for an internal correlation of these quantities within halos.

4.6. Filament Directions in Methods I and II

Throughout the paper we find very good agreement between various alignment signals for Methods I and II, however, it is not necessary that the same halos in the two methods have the same filament directions. In order to make a more profound understanding of the agreement results of the two methods, we compute the probability distribution $P(\cos\theta)$ of the angle between the directions of the filaments from Method I and the filament vectors from Method II. As shown in Figure 16, the filament directions for the same halos in the two methods agree very well and more than 60% halos have $\theta \sim 0$. In addition, we did not find any significant halo mass dependence for these filament angles. As we have also checked the local density and distance to the most massive node halo of each common halo, we do not find any significant dependence on this angle θ.
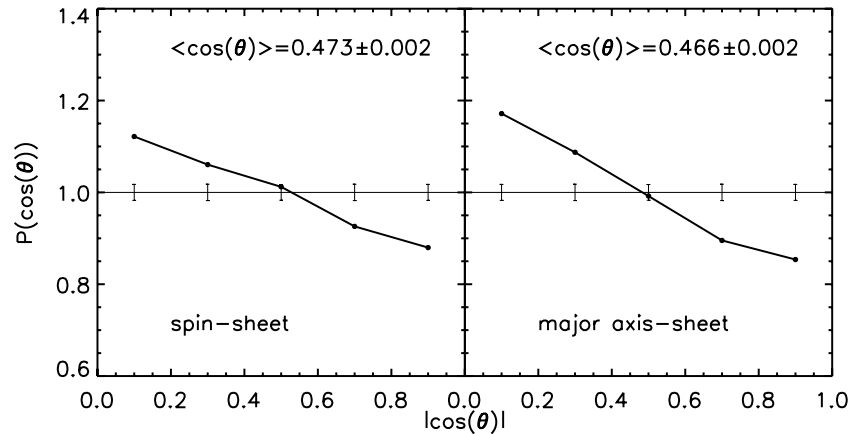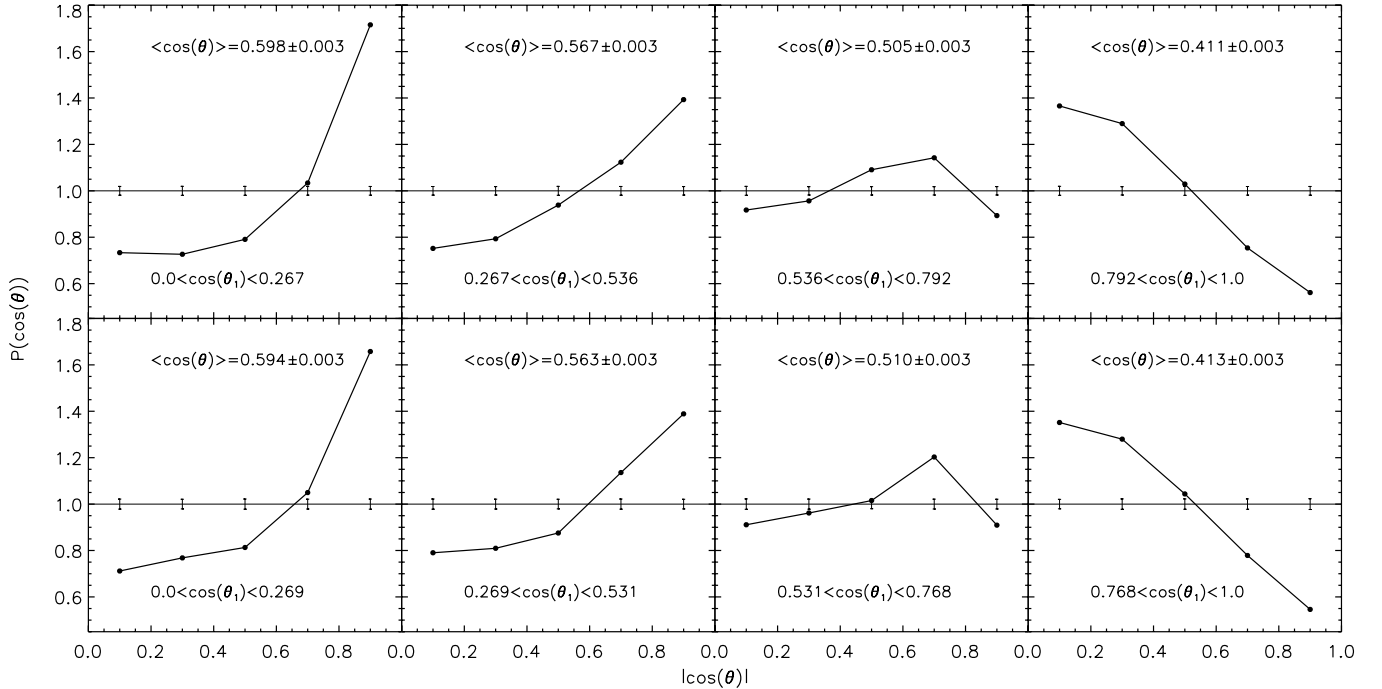

Figure 13. Left panel: probability distribution of the cosine of the angle between the halo angular momentum vector and the vector perpendicular to the sheet in Method I. Right panel: same as the left panel but for the halo major axis vector.
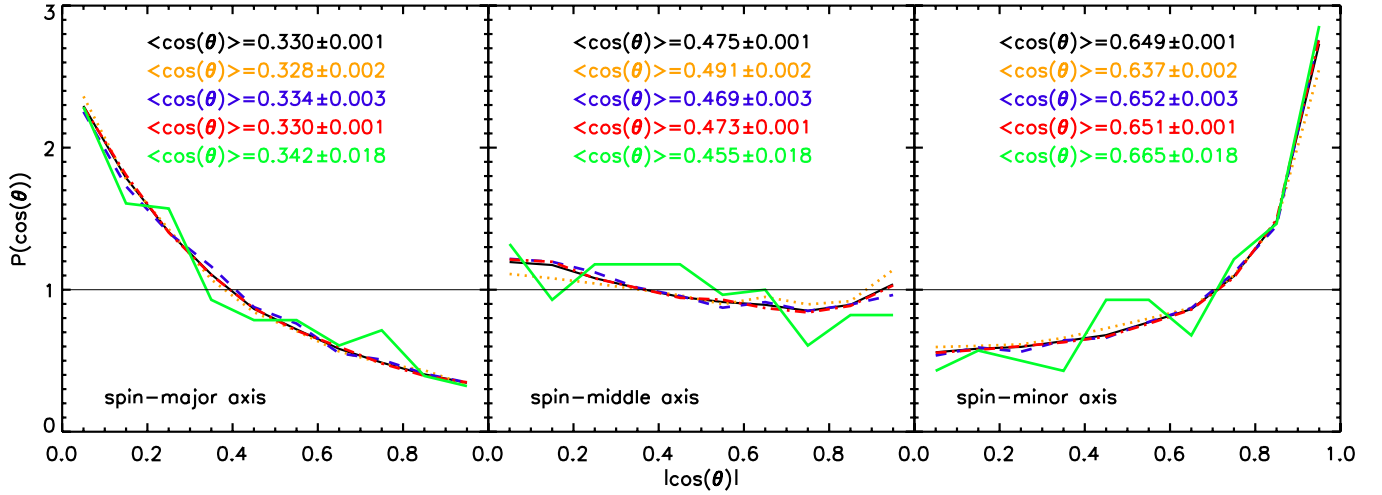
Figure 14. Probability distribution of the cosine of the angle between the angular momentum and major (left panel), middle (middle panel), and minor (right panel) axis vectors of the halos in clusters (orange dotted), filaments (red dash-dotted), sheets (blue dashed), and voids (green dash-dot-dot). The black solid line indicates the values for all the halos in our halo catalog.

(A color version of this figure is available in the online journal.)

Figure 15. Probability distribution of the cosine of the angle between the halo spin axis vectors and the directions of the filaments in Methods I (upper panels) and II (lower panels). Each panel from left to right corresponds to 1/4 of the halos in the filaments, ranked according to the cosine of the angle between the halo major axis and the direction of the filaments, $\cos(\theta_1)$. In each panel, the corresponding range of $\cos(\theta_1)$ and the average value of $\langle\cos(\theta)\rangle$ are indicated.

5. SUMMARY

Using the dark matter and halo distributions from a high-resolution *N*-body simulation, we have identified the filamentary structures in the cosmic web using two different filament-finding algorithms. The first method is based on the Hessian matrix of the density field (Method I), where the halos are classified into four categories according to the signs of the three eigenvalues of the Hessian matrix: clusters, filaments, sheets, and voids. The advantage of this method is that the large-scale environments of the halos can be characterized unambiguously, and that there is only one free parameter in the analysis. However, this method needs detailed information about the local density field, which is difficult but not impossible to obtain based on observations. Indeed, some recent studies are devoted to density field reconstructions based on galaxy and halo distributions (e.g., Erdogdu et al. 2006 from 2MASS Redshift Survey; and Wang et al. 2009a from halo distribution in simulations).

On the other hand, Method II directly uses the distribution of halos. Thus, it eliminates the need for a reconstruction of the local mass density field, at the price of a larger number of tunable parameters. Filamentary structures are here traced by connecting single segments which are identified according to their relative mass over-density. In this study, we were not interested in explicitly reconstructing long coherent filaments, rather we only explore the orientations of the segments relative to the
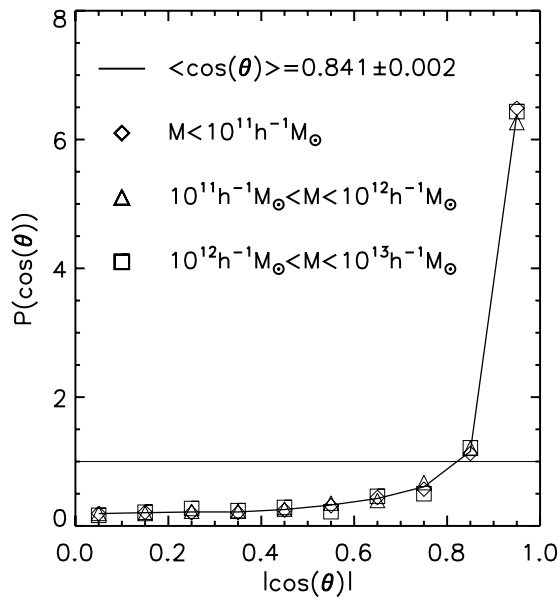
Figure 16. Probability distribution of the cosine of the angle between the directions of the filaments from Method I and the filament vectors from Method II for all the filament halos (black solid) and different mass range of halos. The average value of $\cos\theta$ of all the filament halos is also shown.

gravitational potential field (instead of the density field), and also found an opposite mass dependence for the alignment strength of spin– and shape–filament alignments. Moreover, they found that the spin axes of halos with mass $\geqslant 10^{13} \ h^{-1} M_\odot$ are preferentially perpendicular to the filament directions, which we cannot confirm in this study because of the limited volume of our simulation. A similar behavior has been detected by Aragón-Calvo et al. (2007b) using a multi-scale morphology filter method for the classification of the large-scale environments.

Quite interestingly, we find in Method II according to the spin and shape alignment signals of the halos in the filaments, there is a transit influence scale of large-scale environments: from the two-dimensional collapse phase of the filament to the three-dimensional collapse phase of the cluster/node halo at small separation to the most massive node halo.

The general trends found from our *N*-body simulation reveal a substantial interplay between the large-scale environments and the internal properties of the dark matter halos. It would be interesting to see whether similar trends can be observed in real galaxy samples (e.g., Lee & Pen 2001; Lee & Erdogdu 2007). The two methods outlined in this study should be straightforward applicable to observational data sets (e.g., SDSS). This should be provided for interesting tests of galaxy formation models, and of cold dark matter cosmologies.

halos orientations associated with them. The main shortcomings of Method II are the relatively large number of parameters and a lack of sensitivity for the detection of less prominent filaments. Nevertheless, Method II is easy to implement on top of observational data, including also galaxy group catalogs such as that of Yang et al. (2007). This makes it a highly useful approach in practice, provided its results are consistent with those obtained with Method I. This is indeed the case, as we have demonstrated in this study. Moreover, in Method II, halos are automatically grouped into filaments, and we know what halo belongs to what filament.

Based on the classification of the large-scale environment around halos that we obtained, we examined the spin-filament and the shape–filament alignments, as well as the corresponding quantities for halos and sheets. Overall, we find a tendency for halo spins and shapes to be oriented parallel to filaments and perpendicular to the normal vector of sheet-like structures. This trend becomes obvious and is clearly significant when compared to results from isotropic (randomized) orientations. Both the spin and shape alignment strength are stronger for halos close to more massive node (cluster) halos, and at smaller separations to the node halos. Yet, the spin and shape alignment strength show an opposite mass dependence: smaller halos display stronger (weaker) spin (shape) alignments with the filaments.

For the halos in different environments, we have also investigated their intrinsic spin–shape alignment. We found that the spin axes are preferentially aligned with the minor axes of halos, and are perpendicular to the major axes, independent of the halo environments. At first glance, this result seems to be at odds with our finding that *both* the spin and major axes tend to align with the filament directions. However, there is not really a contradiction here, because the alignments *are not perfect* in both cases. In fact, the distributions of the alignment angles are sufficiently broad that both of these seemingly contradictory alignment signals can coexist.

Our results are in good agreement with recent *N*-body studies where different filament finding methods have been employed. Hahn et al. (2007a) applied a Hessian matrix approach to the

REFERENCES

Allgood, B., Flores, R. A., Primack, J. R., Kravtsov, A. V., Wechsler, R. H., Faltenbacher, A., & Bullock, J. S. 2006, MNRAS, 367, 1781
Altay, G., Colberg, J. M., & Croft, R. A. C. 2006, MNRAS, 370, 1422
Aragón-Calvo, M. A., Jones, B. J. T., van de Weygaert, R., & van der Hulst, J. M. 2007a, A&A, 474, 315
Aragón-Calvo, M. A., van de Weygaert, R., Jones, B. J. T., & van der Hulst, J. M. 2007b, ApJ, 655, L5
Avila-Reese, V., Colín, P., Gottlöber, S., Firmani, C., & Maulbetsch, C. 2005, ApJ, 634, 51
Bailin, J., & Steinmetz, M. 2005, ApJ, 627, 647
Barrow, J. D., Bhavsar, S. P., & Sonoda, D. H. 1985, MNRAS, 216, 17
Bond, J. R., Kofman, L., & Pogosyan, D. 1996, Nature, 380, 603
Bett, P., Eke, V., Frenk, C. S., Jenkins, A., Helly, J., & Navarro, J. 2007, MNRAS, 376, 215
Brunino, R., Trujillo, R., Pearce, F. R., & Thomas, P. A. 2007, MNRAS, 375, 184
Colberg, J. M. 2007, MNRAS, 375, 337
Colberg, J. M., Krughoff, K. S., & Connolly, A. J. 2005, MNRAS, 359, 272
Colberg, J. M., et al. 2009, MNRAS, 387, 933
Cooper, M. C., et al. 2007, MNRAS, 376, 1445
Croton, D. J., Gao, L., & White, S. D. M. 2007, MNRAS, 374, 1303
Dalal, N., White, M., Bond, J. R., & Shirokov, A. 2008, ApJ, 687, 12
Davis, M., Efstathiou, G., Frenk, C. S., & White, S. D. M. 1985, ApJ, 292, 371
Doroshkevich, A. G. 1970, Astrophysics, 6, 320
Eke, V. R., et al. 2004, MNRAS, 348, 866
Erdogdu, P., et al. 2006, MNRAS, 373, 45
Faltenbacher, A., Gottlöber, S., Kerscher, M., & Müller, V. 2002, A&A, 395, 1
Faltenbacher, A., Jing, Y. P., Li, C., Mao, S., Mo, H. J., Pasquali, A., & van den Bosch, F. C. 2008, ApJ, 675, 146
Forero-Romero, J. E., Hoffman, Y., Gottloeber, S., Klypin, A., & Yepes, G. 2009, MNRAS, 396, 1815
Gao, L., Springel, V., & White, S. D. M. 2005, MNRAS, 363, L66

Gao, L., & White, S. D. M. 2007, MNRAS, 377, L5
Gott, J. R., III, Dickinson, M., & Melott, A. L. 1986, ApJ, 306, 341
Hahn, O., Carollo, C. M., Porciani, C., & Dekel, A. 2007a, MNRAS, 381, 41
Hahn, O., Porciani, C., Carollo, C. M., & Dekel, A. 2007b, MNRAS, 375, 489
Hahn, O., Porciani, C., Dekel, A., & Carollo, C. M. 2009, MNRAS, 398, 1742
Hoyle, F., & Vogeley, M. 2002, ApJ, 580, 663
Lee, J. 2004, ApJ, 614, L1
Lee, J., & Erdogdu, P. 2007, ApJ, 671, 1248
Lee, J., & Pen, U. L. 2001, ApJ, 555, 106
Macciò, A. V., Dutton, A. A., van den Bosch, F. C., Moore, B., Potter, D., &
    Stadel, J. 2007, MNRAS, 378, 55
Mecke, K. R., Buchert, T., & Wagner, H. 1994, A&A, 288, 697
Navarro, J. F., Abadi, M. G., & Steinmetz, M. 2004, ApJ, 613, L41
Novikov, D., Colombi, S., & Doré, O. 2006, MNRAS, 366, 1201
Pandey, B., & Bharadwaj, S. 2008, MNRAS, 387, 767
Paz, D., Stasyszyn, F., & Padilla, N. 2008, MNRAS, 389, 1127
Peebles, P. J. E. 1969, ApJ, 155, 393
Peebles, P. J. E. 1980, The Large-scale Structure of the Universe (Princeton, NJ:
    Princeton Univ. Press)
Pereira, M. J., Bryan, G. L., & Gill, S. P. D. 2008, ApJ, 672, 825
Pimbblet, K. A. 2005, MNRAS, 358, 256
Porciani, C., Dekel, A., & Hoffman, Y. 2002, MNRAS, 332, 325
Reed, D. S., Governato, F., Quinn, T., Stadel, J., & Lake, G. 2007, MNRAS,
    378, 777
Sahni, V., Sathyaprakash, B. S., & Shandarin, S. F. 1998, ApJ, 495, 5
Schaap, W. E., & van de Weygaert, R. 2000, A&A, 363, L29

Schmalzing, J., et al. 1999, ApJ, 526, 568
Sheth, R. K., Mo, H. J., & Tormen, G. 2001, MNRAS, 323, 1
Sheth, R. K., & Tormen, G. 2004, MNRAS, 350, 1385
Sousbie, T., Pichon, C., Colombi, S., Novikov, D., & Pogosyan, D. 2008,
    MNRAS, 383, 1655
Springel, V., Yoshida, N., & White, S. D. M. 2001, New Astron., 6, 79
Springel, V., et al. 2005, Nature, 435, 629
Stoica, R. S., Martínez, V. J., Mateu, J., & Saar, E. 2005, A&A, 434, 423
Stoica, R. S., Martínez, V. J., & Saar, E. 2007, Appl. Stat., 56, 459
Wang, H. Y., Mo, H. J., & Jing, Y. P. 2007, MNRAS, 375, 633
Wang, H. Y., Mo, H. J., Jing, Y. P., Guo, Y., van den Bosch, F. C., & Yang, X.
    2009a, MNRAS, 394, 398
Wang, Y., Yang, X., Mo, H. J., van den Bosch, F. C., Katz, N., Pasquali, A.,
    McIntosh, D. H., & Weinmann, S. M. 2009b, ApJ, 697, 247
Wang, Y., Yang, X., Mo, H. J., van den Bosch, F. C., Weinmann, S. M., & Chu,
    Y. 2008, ApJ, 687, 919
Wechsler, R. H., Zentner, A. R., Bullock, J. S., Kravtsov, A. V., & Allgood, B.
    2006, ApJ, 652, 71
White, S. D. M. 1984, ApJ, 286, 38
Yang, X., Mo, H. J., & van den Bosch, F. C. 2006, ApJ, 638, L55
Yang, X., Mo, H. J., & van den Bosch, F. C. 2009, ApJ, 693, 830
Yang, X., Mo, H. J., van den Bosch, F. C., & Jing, Y. P. 2005, MNRAS, 356,
    1293
Yang, X., Mo, H. J., van den Bosch, F. C., Pasquali, A., Li, C., & Barden, M.
    2007, ApJ, 671, 153
York, D., et al. 2000, AJ, 120, 1579